AIAA JOURNAL
Vol. 32, No. 1, January 1994

Effect of Artificial Viscosity on Three-Dimensional Flow Solutions

Eli Turkel*
Tel-Aviv University, Tel-Aviv, Israel
and
Veer N. Vatsa†
NASA Langley Research Center, Hampton, Virginia 23681

Artificial viscosity is added either implicitly or explicitly in practically every numerical scheme for suppressing spurious oscillations in the solution of fluid-dynamics equations. In the present central-difference scheme, artificial viscosity is added explicitly for suppressing high-frequency oscillations and achieving good convergence properties. The amount of artificial viscosity added is controlled through the use of preselected coefficients. In the standard scheme, scalar coefficients based on the spectral radii of the Jacobian of the convective fluxes are used. However, this can add too much viscosity to the slower waves. Hence, the use of matrix-valued coefficients, which give appropriate viscosity for each wave component, is suggested. With the matrix-valued coefficients, the central-difference scheme produces more accurate solutions on a given grid, particularly in the vicinity of shocks and boundary layers, while still maintaining good convergence properties.

Introduction

SIGNIFICANT progress has been made in recent years toward the computation of transonic viscous flows over aircraft components. Despite significant gains in the raw speed of modern computers, most numerical schemes still require prohibitive amounts of computer time to obtain accurate solutions of the Navier-Stokes equations. The large amounts of computer time required for obtaining grid-converged solutions makes it a difficult and extremely time-consuming exercise to assess numerical accuracy of the solutions. Additionally, the researchers are discouraged from investigating more sophisticated turbulence models, since these invariably add significantly to the computational time.

Recently, an efficient numerical procedure for computing high Reynolds number, viscous, transonic, three-dimensional flows over aircraft components has been developed by Vatsa and Wedan.[1] In this procedure, the Runge-Kutta time-stepping scheme developed by Jameson and co-workers for the Euler equations[2,3] is used as the basic algorithm. Significant improvement in the efficiency of the algorithm is obtained through the use of a multigrid acceleration technique patterned after the work of Martinelli[4] and Swanson and Turkel[5] for two-dimensional viscous flows. The details of the three-dimensional extension of the two-dimensional schemes of Refs. 4 and 5 are given in Ref. 1.

Based on the work of Vatsa and Wedan,[1] it is clear that essentially grid-converged solutions for transonic viscous flows over aerodynamic shapes can be obtained, provided sufficiently fine meshes are employed for computation. In the present paper, an attempt is made to improve the accuracy of the solutions on a given grid, in order to reduce the number of grid points required for obtaining a specified level of accuracy. This is done mainly through the reduction of artificial viscosity by replacing the scalar form of the artificial viscosity used in Ref. 1 with a matrix form deduced by employing concepts from upwind schemes. Computational results based on the use of matrix-valued dissipation are very encouraging and are compared with scalar dissipation results in this paper for transonic flow over finite wings.

Received March 9, 1992; revision received Oct. 5, 1992; accepted for publication March 11, 1993.

*Visiting Scientist, ICASE, Hampton, VA.
†Senior Research Scientist. Member AIAA.

Governing Equations and Numerical Method

In the present investigation, the thin-layer Navier-Stokes (TLNS) equations are used for modeling the flow. TLNS as used here describes an equation set obtained by retaining the viscous diffusion normal to the body surface only. The effects of turbulence are modeled through an eddy-viscosity hypothesis. The Baldwin-Lomax turbulence model[6] is used for turbulence closure. For a body-fitted coordinate system (ξ, η, ζ) fixed in time, these equations can be written in the conservation law form as

$$\frac{\partial}{\partial t}(J^{-1}U) + \frac{\partial F}{\partial \xi} + \frac{\partial G}{\partial \eta} + \frac{\partial H}{\partial \zeta} = \frac{\partial G_v}{\partial \eta} \tag{1}$$

where U represents the conserved variable vector, and F, G, and H represent the convective flux vectors. G_v in the foregoing equation represents the viscous flux vector in the surface normal direction and J is the Jacobian of the transformation. The complete form of the flux vectors is readily available in Ref. 1 and is skipped here for the sake of brevity. The convective terms can also be written as

$$\frac{\partial F}{\partial \xi} = \boldsymbol{A}\frac{\partial U}{\partial \xi} \tag{2}$$

$$\frac{\partial G}{\partial \eta} = \boldsymbol{B}\frac{\partial U}{\partial \eta} \tag{3}$$

$$\frac{\partial H}{\partial \zeta} = \boldsymbol{C}\frac{\partial U}{\partial \zeta} \tag{4}$$

where $\boldsymbol{A} = \partial F/\partial U$, $\boldsymbol{B} = \partial G/\partial U$, and $\boldsymbol{C} = \partial H/\partial U$ are known as the flux Jacobian matrices.

A semidiscrete cell-centered finite-volume algorithm based on a Runge-Kutta time-stepping scheme[2,3] is used for obtaining the steady-state solutions to the TLNS equations. A linear fourth-difference and nonlinear second-difference-based artificial dissipation is added to the present central-difference scheme to suppress odd-even decoupling and oscillations in the vicinity of shock waves and stagnation points. The artificial viscosity models under consideration will be discussed in a later section.

A five-stage Runge-Kutta time-stepping scheme with three evaluations of the artificial dissipation terms (computed at the odd stages) is used to extend the stability bound along the real axis, thus permitting a higher CFL number in the presence of physical viscous diffusion terms. To further extend the stability range of the numerical scheme, the implicit residual smoothing technique of Ref. 2, as modified by Martinelli[4] for high-aspect-ratio cells, is extended to three-dimensional flows. Since we are basically interested in obtaining steady-state results, the solution is advanced in time with the maximum allowable time step for each cell. Enthalpy damping, which was used in previous studies for accelerating the convergence of the scheme, is not employed in the present calculations. This is more consistent with the governing equations, since the Navier-Stokes equations for general flows do not admit constant enthalpy as a solution. The efficiency of the numerical scheme is greatly enhanced through the use of a multigrid acceleration technique as described by Vatsa and Wedan.[1]

Artificial Dissipation Models

Since the basic numerical scheme uses central differences to represent spatial derivatives, the artificial dissipation required to avoid spurious oscillations in the vicinity of shocks and to stabilize the scheme is implemented in a convenient manner by modifying the convective fluxes as follows:

$$F_{i\pm\frac{1}{2},j,k} = \tfrac{1}{2}(F_{i,j,k} + F_{i\pm1,j,k}) - d_{i\pm\frac{1}{2},j,k} \tag{5}$$

$$G_{i,j\pm\frac{1}{2},k} = \tfrac{1}{2}(G_{i,j,k} + G_{i,j\pm1,k}) - d_{i,j\pm\frac{1}{2},k} \tag{6}$$

$$H_{i,j,k\pm\frac{1}{2}} = \tfrac{1}{2}(H_{i,j,k} + H_{i,j,k\pm1}) - d_{i,j,k\pm\frac{1}{2}} \tag{7}$$

The terms $d_{i\pm\frac{1}{2},j,k}$, $d_{i,j\pm\frac{1}{2},k}$, and $d_{i,j,k\pm\frac{1}{2}}$ represent the dissipative terms in the i, j, and k directions, respectively. The two forms of artificial dissipation models used in this paper to evaluate these terms are now described.

A. Scalar Dissipation Model

The basic dissipation model employed in this study is a nonisotropic model, in which the dissipative terms are functions of the spectral radii of the Jacobian matrices associated with the appropriate coordinate directions.[1,4,5] For clarity, a detailed description of the dissipative terms for the i direction is given as

$$d_{i+\frac{1}{2},j,k} = \lambda_{i+\frac{1}{2},j,k}[\epsilon^{(2)}_{i+\frac{1}{2},j,k}(W_{i+1,j,k} - W_{i,j,k}) - \epsilon^{(4)}_{i+\frac{1}{2},j,k}(W_{i+2,j,k} - 3W_{i+1,j,k} + 3W_{i,j,k} - W_{i-1,j,k})] \tag{8}$$

In the foregoing expression, the coefficients $\epsilon^{(2)}$ and $\epsilon^{(4)}$ are related to the pressure gradient parameter ν_i as follows:

$$\nu_i = \frac{|p_{i+1,j,k} - 2p_{i,j,k} + p_{i-1,j,k}|}{p_{i+1,j,k} + 2p_{i,j,k} + p_{i-1,j,k}}$$

$$\epsilon^{(2)}_{i+\frac{1}{2},j,k} = \kappa^{(2)} \max(\nu_{i+1}, \nu_i) \tag{9}$$

$$\epsilon^{(4)}_{i+\frac{1}{2},j,k} = \max\{0, [\kappa^{(4)} - \epsilon^{(2)}_{i+\frac{1}{2},j,k}]\}$$

where $\kappa^{(2)}$ and $\kappa^{(4)}$ are constants with typical values of $\frac{1}{2}$ and $\frac{1}{64}$, respectively. The variable W is related to the solution vector U by the equation

$$W = U + [0, 0, 0, 0, p]^T \tag{10}$$

The term $\lambda_{i+\frac{1}{2},j,k}$ is the scaling factor associated with the ξ coordinate. Following Refs. 4 and 5, this scale factor is defined as

$$\lambda_{i+\frac{1}{2},j,k} = \tfrac{1}{2}[(\bar{\lambda}_\xi)_{i,j,k} + (\bar{\lambda}_\xi)_{i+1,j,k}] \tag{11}$$

where $\bar{\lambda}_\xi$ is related to the spectral radii of the flux Jacobian matrix in the three coordinate directions[1] as follows:

$$(\bar{\lambda}_\xi) = (\lambda_\xi)\left[1 + \left(\frac{\lambda_\eta}{\lambda_\xi}\right)^{0.5} + \left(\frac{\lambda_\zeta}{\lambda_\xi}\right)^{0.5}\right] \tag{12}$$

The spectral radii for the ξ, η, ζ directions are

$$\lambda_\xi = |q_\xi| + c\sqrt{\xi_x^2 + \xi_y^2 + \xi_z^2}$$

$$\lambda_\eta = |q_\eta| + c\sqrt{\eta_x^2 + \eta_y^2 + \eta_z^2} \tag{13}$$

$$\lambda_\zeta = |q_\zeta| + c\sqrt{\zeta_x^2 + \zeta_y^2 + \zeta_z^2}$$

In the foregoing equations, c is the local speed of sound and q_ξ, q_η, and q_ζ are the contravariant velocity vectors in the i, j, and $k(\xi, \eta, \zeta)$ directions, respectively, and are given by the following relations:

$$q_\xi = \xi_x u + \xi_y v + \xi_z w$$

$$q_\eta = \eta_x u + \eta_y v + \eta_z w \tag{14}$$

$$q_\zeta = \zeta_x u + \zeta_y v + \zeta_z w$$

Expressions for the artificial dissipation coefficients in the j and k directions can be derived in a similar manner[1] and take the form

$$(\bar{\lambda}_\eta) = (\lambda_\eta)\left[1 + \left(\frac{\lambda_\xi}{\lambda_\eta}\right)^{0.5} + \left(\frac{\lambda_\zeta}{\lambda_\eta}\right)^{0.5}\right] \tag{15}$$

$$(\bar{\lambda}_\zeta) = (\lambda_\zeta)\left[1 + \left(\frac{\lambda_\xi}{\lambda_\zeta}\right)^{0.5} + \left(\frac{\lambda_\eta}{\lambda_\zeta}\right)^{0.5}\right] \tag{16}$$

B. Matrix-Valued Dissipation

The dissipation model just described is not optimal in the sense that the same dissipation scaling is used for all the governing equations in a given coordinate direction. Reduced artificial dissipation can be obtained by individually scaling the dissipation contribution to each equation, as is done implicitly in upwind schemes. This is done by replacing the scalar coefficients used in the artificial dissipation model by the modulus (absolute values) of flux Jacobian matrices. Thus, Eqs. (12–16) can be rewritten as

$$\bar{\lambda}_\xi = |A|, \qquad \bar{\lambda}_\eta = |B|, \qquad \bar{\lambda}_\zeta = |C| \tag{17}$$

The matrices A, B, and C have very few nonzero elements and can be found in Ref. 7 in their entirety. The absolute values of these matrices, illustrated here for the matrix A, are defined in the following manner. Let

$$A = T_\xi \Lambda_\xi T_\xi^{-1} \tag{18}$$

where Λ_ξ is a diagonal matrix with the eigenvalues of A as its elements. Then

$$|A| = T_\xi |\Lambda_\xi| T_\xi^{-1} \tag{19}$$

where

$$|A_\xi| = \begin{bmatrix} |\lambda_1| & 0 & 0 & 0 & 0 \\ 0 & |\lambda_2| & 0 & 0 & 0 \\ 0 & 0 & |\lambda_3| & 0 & 0 \\ 0 & 0 & 0 & |\lambda_3| & 0 \\ 0 & 0 & 0 & 0 & |\lambda_3| \end{bmatrix} \tag{20}$$

The diagonal elements of the foregoing matrix[7] are

$$\lambda_1 = q_\xi + c\sqrt{\xi_x^2 + \xi_y^2 + \xi_z^2}$$

$$\lambda_2 = q_\xi - c\sqrt{\xi_x^2 + \xi_y^2 + \xi_z^2} \tag{21}$$

$$\lambda_3 = q_\xi$$

After considerable algebra, one can express $|A|$ in the following manner:

$$|A| = |\lambda_3| I + \left(\frac{|\lambda_1| + |\lambda_2|}{2} - |\lambda_3|\right) \times \left[\frac{(\gamma-1)}{c^2} E_1 + \frac{E_2}{\xi_x^2 + \xi_y^2 + \xi_z^2}\right] + \frac{|\lambda_1| - |\lambda_2|}{[2c\sqrt{\xi_x^2 + \xi_y^2 + \xi_z^2}]} \times [E_3 + (\gamma - 1)E_4] \tag{22}$$

In the previous equations, $E_1 - E_4$ are 5×5 matrices and I is the identity matrix of the same size. By taking advantage of their special form, these matrices can be expressed as a product of the four row vectors (and their transposes) in the following manner:

$$E_1 = R_1^T R_2, \quad E_2 = R_3^T R_4, \quad E_3 = R_1^T R_4, \quad E_4 = R_3^T R_2 \tag{23}$$

where

$$R_1 = \{1, u, v, w, h\} \qquad R_2 = \{V_t^2/2, -u, -v, -w, 1\} \tag{24}$$

$$R_3 = \{0, \xi_x, \xi_y, \xi_z, q_\xi\} \qquad R_4 = \{-q_\xi, \xi_x, \xi_y, \xi_z, 0\} \tag{25}$$

and $V_t^2 = u^2 + v^2 + w^2$ is the total velocity.

Thus, by taking advantage of the special form of the elements of $|A|$, one can replace the matrix-vector products of the form $|A|\,(W_{i+1,j,k} - W_{i,j,k})$ by the products of row and column vectors, resulting in a simpler and more efficient procedure.

In practice, we cannot choose $\lambda_1, \lambda_2, \lambda_3$ as given by Eq. (21). Near-stagnation points λ_3 approach zero, whereas near sonic lines λ_1 or λ_2 approach zero. Since zero artificial viscosity can create numerical difficulties, we limit these values in the following manner:

$$|\tilde{\lambda}_1| = \max(|\lambda_1|, V_n\lambda_\xi)$$

$$|\tilde{\lambda}_2| = \max(|\lambda_2|, V_n\lambda_\xi) \tag{26}$$

$$|\tilde{\lambda}_3| = \max(|\lambda_3|, V_l\lambda_\xi)$$

where V_n limits the eigenvalues associated with the nonlinear characteristic fields to a minimum value that is a fraction of the spectral radius, whereas V_l provides a similar limiter for the eigenvalues associated with the linear characteristic fields. The values for the limiting coefficients V_n and V_l are determined through numerical experimentation such that sharper shocks and suction peaks are captured without introducing spurious oscillations in the solution and still maintaining good convergence properties. It should be noted that by setting $V_n = V_l = 1$, we recover the scalar form of the artificial dissipation, whereas setting $V_n = V_l = 0$ corresponds to the use of actual eigenvalues without any limiters. The eigenvalues obtained from Eq. (26) are then modified for large changes in cell aspect ratios using the expressions given in Eq. (12). Similar expressions can be derived for the matrices B and C by replacing the contravariant velocity q_ξ by q_η and q_ζ, and ξ by η and ζ, respectively, in Eqs. (17–25).

The following procedure is adopted at the boundaries where the central-difference operators required to form the dissipation terms cannot be evaluated in a straightforward manner. Near the far-field and downstream boundaries, information on the flow variables at the auxiliary cells (ghost cells) that surround these boundaries is used to construct the appropriate derivatives. Near the solid boundaries, the linear variation of flow variables is implied in forming the derivatives needed for the dissipative terms, which results in zero dissipative flux at the solid boundaries.[5]

We note that if the dissipative fluxes are interpreted as modifiers to the physical fluxes at the interfaces of the difference molecule, the central-difference scheme with the matrix dissipation closely resembles the characteristic decomposition used in upwind schemes.[8,9] It will be shown in the next section that this scheme is comparable to upwind TVD schemes in accuracy. In addition, when coupled with a multigrid acceleration technique, only a slight degradation in the convergence rate and computational efficiency is observed for this modified scheme, as compared to the original central-difference scheme in which a scalar dissipation model was employed.

Results and Discussion

In order to study the effect of the artificial dissipation models discussed in the previous sections, solutions for transonic, turbulent flow over two different configurations, representing transport and fighter type of wings, are presented. In these computations, C-O grid topologies are used in order to accurately simulate the flow in the wing-tip region. The test cases selected for this paper have extensive pressure data available for code validation.

The first test case selected for this study is that of flow over the ONERA M6 wing at free-stream Mach number $M_\infty = 0.84$, angle of attack $\alpha = 3.06$ deg, and free-stream Reynolds number based on mean aerodynamic chord, $Re_{\bar{c}} = 11.7 \times 10^6$. This case has the geometric characteristics of a typical transport wing and has been the subject of several numerical studies in the past due to the availability of reliable surface pressure data.[10] Solutions were obtained for this case on four successively finer meshes consisting of $97 \times 25 \times 17$, $145 \times 33 \times 25$, $193 \times 49 \times 33$, and $289 \times 65 \times 49$ grid points in the streamwise, normal, and spanwise directions, respectively. The results on the coarsest mesh ($97 \times 25 \times 17$) are omitted from some of the figures to avoid overcrowding.

The second configuration selected for this study is the Lockheed Wing C,[11] which is a highly swept, highly tapered, and low-aspect-ratio wing, typical of a fighter wing. This wing is made of flat-topped supercritical airfoil sections with an approximate 8.17 deg twist from root to tip sections. The transonic flow over this wing is very sensitive due to these physical characteristics and hence a finer mesh density compared to the ONERA M6 wing is required for obtaining grid-converged solutions for this case. Therefore, three meshes consisting of $161 \times 33 \times 33$, $241 \times 49 \times 49$, and $321 \times 65 \times 65$ grid points in the streamwise, normal, and spanwise directions, respectively, were used for this case. Another complicating factor for this case arose because of the presence of significant wall interference effects in the experimental study of Hinson and Burdges.[11] Due to these difficulties, previously available numerical solutions for this configuration have been less than satisfactory. The nominal test conditions chosen for this study are $M_\infty = 0.8513$, $\alpha = 4.9$ deg, and $Re_{\bar{c}} = 10^7$. By making use of the guidelines provided in Ref. 11 and some preliminary wall interference estimates based on the method of Ref. 12, the calculations were performed at $M_\infty = 0.8427$ and $\alpha = 4$ deg.

A. Pressure Distributions

Computed pressure distributions using the scalar and matrix dissipation models are compared with the experimental data in Figs. 1 and 2 for the ONERA M6 and Lockheed Wing C, respectively. Several observations can be made by close examination of the results presented in these figures. First of all, the computational results on the two finest meshes employed in

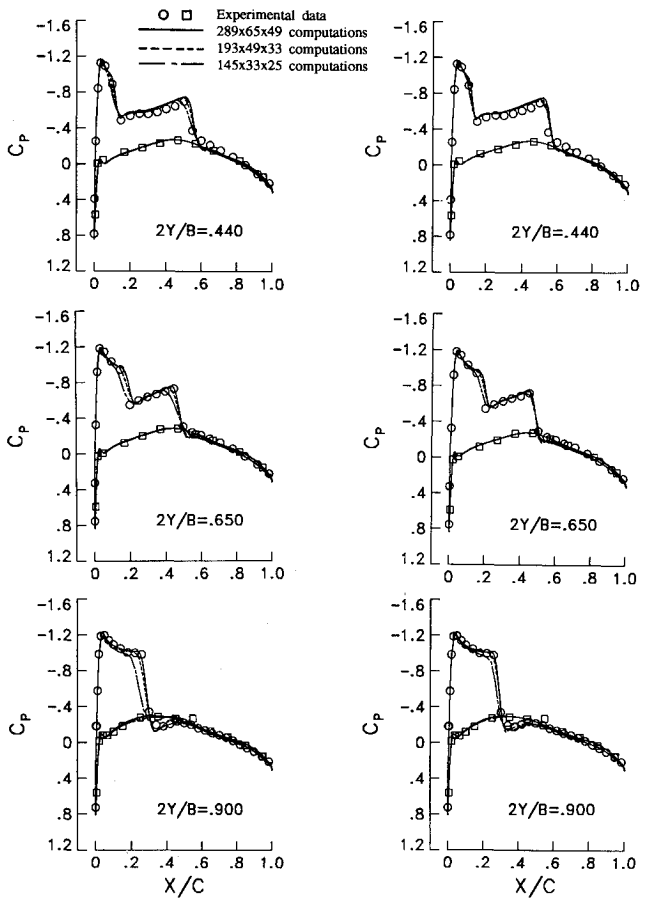

Fig. 1 Effect of grid density on pressure distributions for ONERA M6 wing ($M_\infty = 0.84$, $\alpha = 3.06$ deg, $Re_{\bar{c}} = 11.7 \times 10^6$).

this study are in close agreement with each other and compare well with the experimental data. As expected, the agreement with the data improves with mesh refinement, and the solutions obtained with either of the dissipation models on the finest meshes employed in this study are in excellent agreement with the data and are almost identical to each other. The second observation that can be drawn from these comparisons is that the solutions obtained with the matrix dissipation show less sensitivity to mesh variation and the overall accuracy of the results is improved substantially through the use of the matrix-valued dissipation model. This is more obvious for the coarser meshes, where the results with the matrix dissipation are found to be closer to the fine mesh solutions and experimental data than the corresponding scaler dissipation results. These results indicate that the computed pressure distributions with the matrix dissipation model on the finest meshes are essentially grid converged for both cases considered here.

For the ONERA M6 wing, the computed pressure distributions on the coarse mesh ($145 \times 33 \times 25$) are compared with the results obtained from a "third-order" upwind biased scheme[13] in Fig. 3. On examining this figure, it appears that the solutions obtained with the scalar dissipation model on this mesh indicate significant smearing of shocks, whereas the matrix dissipation results presented here show crisper shocks and are found to be comparable in accuracy to the solutions obtained from a Roe-type upwind difference scheme on the identical mesh. It is also worth mentioning that for these cases, the effect of replacing the arithmetic average with "Roe-averaged"[14] cell-face quantities in the evaluation of Jacobian matrices was insignificant.

B. Lift Coefficient Comparisons

The computed lift coefficients vs the reciprocal of the total number of mesh points raised to two-third power (representing the square of an average mesh density, which should be an appropriate scale for a second-order accurate scheme) are plotted in Fig. 4, in order to further quantify the accuracy level of the computed pressure distributions. Results for both the scalar and matrix dissipation models are shown in this figure. For the ONERA M6 case, the lift coefficient exhibits trends similar to those for the pressure distributions, i.e., less change is observed for the lift coefficient with grid variation for the matrix dissipation as compared to the scalar dissipation case. In addition, a more accurate value for the lift coefficient is obtained for a given grid density by using the matrix dissipation model. Over the range of meshes employed here, the matrix dissipation on a given mesh produces results that are comparable in accuracy to the scalar dissipation results on the next finer mesh, which translates into approximately a factor of 2.6–2.9 reduction in terms of mesh points.

However, the computed lift-coefficient variations for Wing C with matrix dissipation appear to be more sensitive to grid refinement when compared with the results obtained by using the scalar dissipation model. It is believed that this discrepancy arises due to the presence of a weak shock in the leading-edge region at outboard sections of this wing. As seen from the pressure distributions, such a structure was nearly missing on the coarser meshes, particularly with the scalar dissipation model. Better resolution of this shock structure reduces the overall value of the lift coefficient, whereas on the rest of the wing, the lift coefficient increases with mesh refinement. Such compensating effects result in the discrepancy observed here. Nonetheless, the actual values of lift coefficient on the finest mesh ($321 \times 65 \times 65$) obtained from the two different dissipation models differ by less than 0.25%, which is considered to be quite accurate for all practical purposes. Similar trends are obtained for the pitching-moment coefficient (not shown) for these test cases.

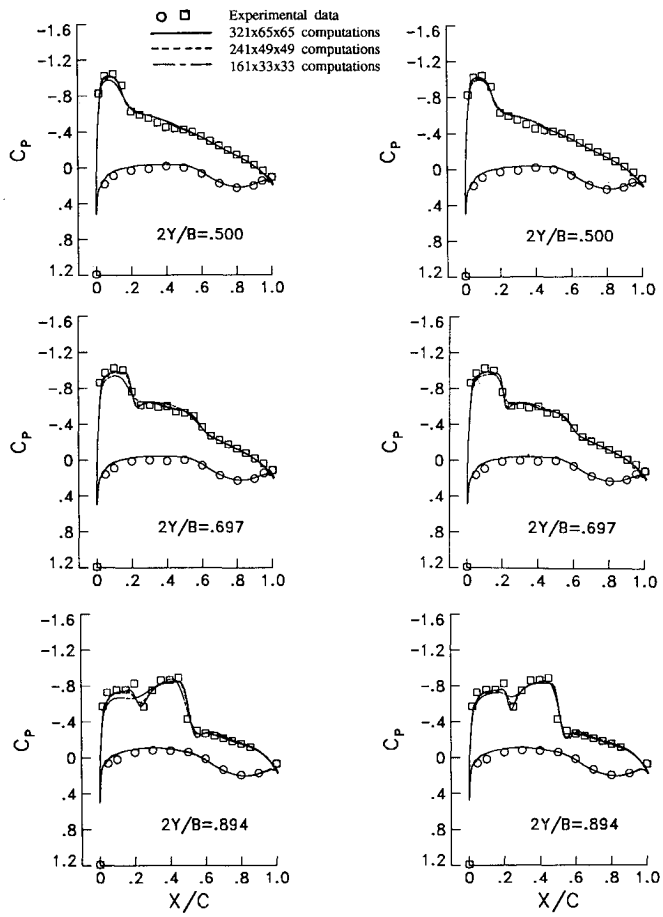

Fig. 2 Effect of grid density on pressure distributions for Lockheed Wing C ($M_\infty = 0.85$, $\alpha = 4.9$ deg, $Re_{\bar{c}} = 10^7$).

C. Skin-Friction Comparisons

Although the pressure distribution is a good indicator of the tangential mesh resolution, it is not indicative of the adequacy of the normal mesh spacing. A better appreciation of the normal mesh resolution is gained through examining the shear stress or skin-friction distribution. This is done in Figs. 5 and 6, where the skin-friction distributions on the upper and lower wing surfaces at the root section are presented for the ONERA M6 and Lockheed Wing C, respectively. A careful examination of these results reveals that the matrix dissipation model on a given mesh density produces more pronounced peaks in the leading-edge region and, in general, predicts higher skin-friction levels on most of the wing surface compared with the scalar dissipation results. In addition, the skin-friction coefficient distributions obtained with the matrix dissipation model

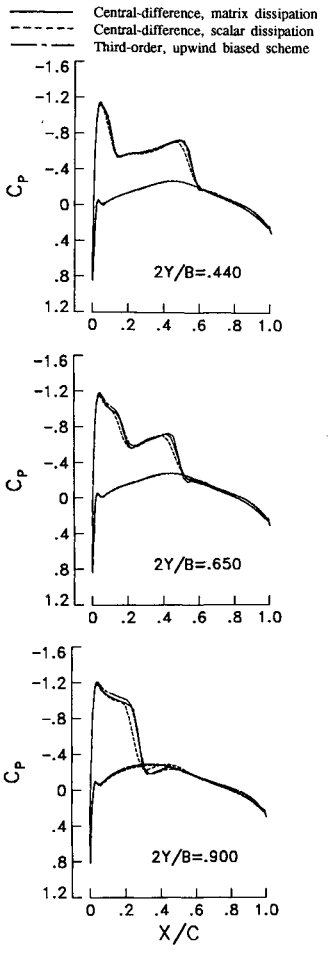

Fig. 3 Comparison of computed pressure distributions on 145 × 33 × 25 grid using central-difference and upwind biased schemes for ONERA M6 wing ($M_\infty = 0.84$, $\alpha = 3.06$ deg, $Re_{\bar{c}} = 11.7 \times 10^6$).

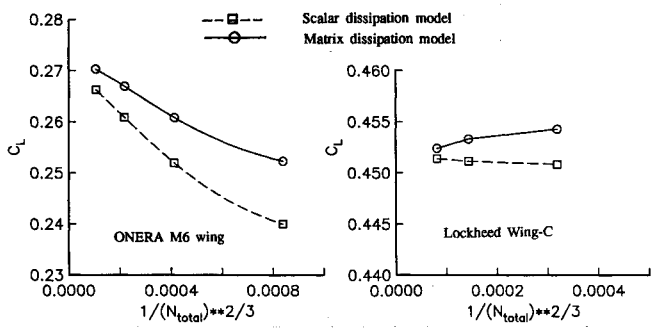

Fig. 4 Variation of lift coefficient with grid density for ONERA M6 and Lockheed Wing C.

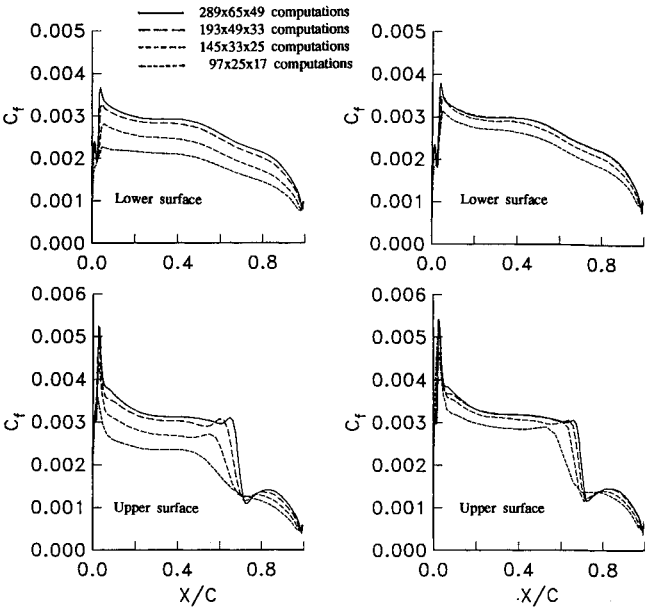

Fig. 5 Variation of root-section surface skin-friction coefficient with grid density for ONERA M6 wing ($M_\infty = 0.84$, $\alpha = 3.06$ deg, $Re_{\bar{c}} = 11.7 \times 10^6$).

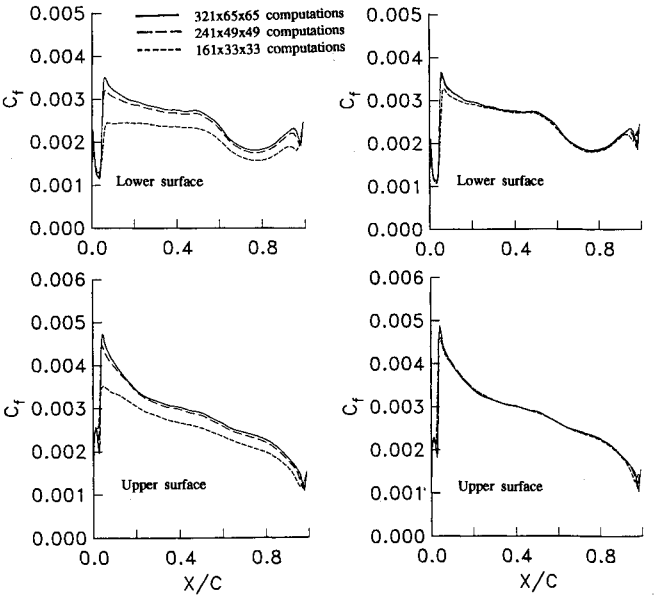

Fig. 6 Variation of root-section surface skin-friction coefficient with grid density for Lockheed Wing C ($M_\infty = 0.85$, $\alpha = 4.9$ deg, $Re_{\bar{c}} = 10^7$).

on the two finest meshes are almost indistinguishable from each other except near shocks. It should be recognized that since a fixed number of cells (about three) are required to capture the shocks in the present scheme, the shocks become sharper with tangential mesh refinement. The fact that the normal mesh spacing employed in these computations is adequate to obtain essentially grid-converged solutions for skin-friction coefficients with the matrix dissipation model is more evident from the results on the lower surface; in this region, the flow is essentially shock-free and the skin-friction distributions on the two finest meshes essentially coalesce. A final note in this context is related to the values of y^+ required to achieve these solutions. All of the solutions presented here were obtained using the Baldwin-Lomax turbulence model and the normal spacings at the wing surface were selected to keep y^+ between 1.5–2.0 on the finest meshes employed here. Solutions obtained with larger wall spacings ($y^+ > 5$) on the

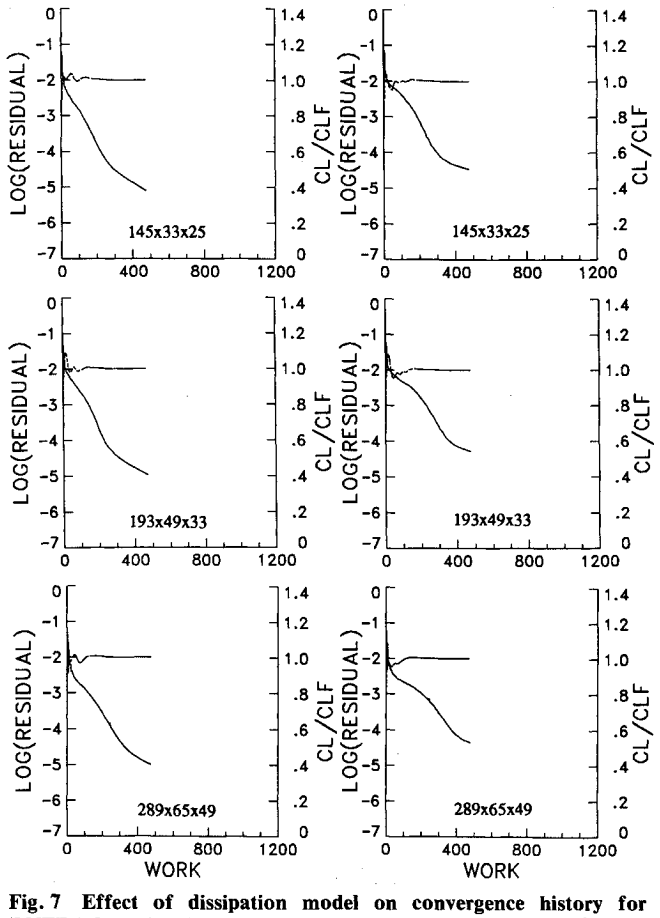

Fig. 7 Effect of dissipation model on convergence history for ONERA M6 wing ($M_\infty = 0.84$, $\alpha = 3.06$ deg, $Re_{\bar{c}} = 11.7 \times 10^6$).

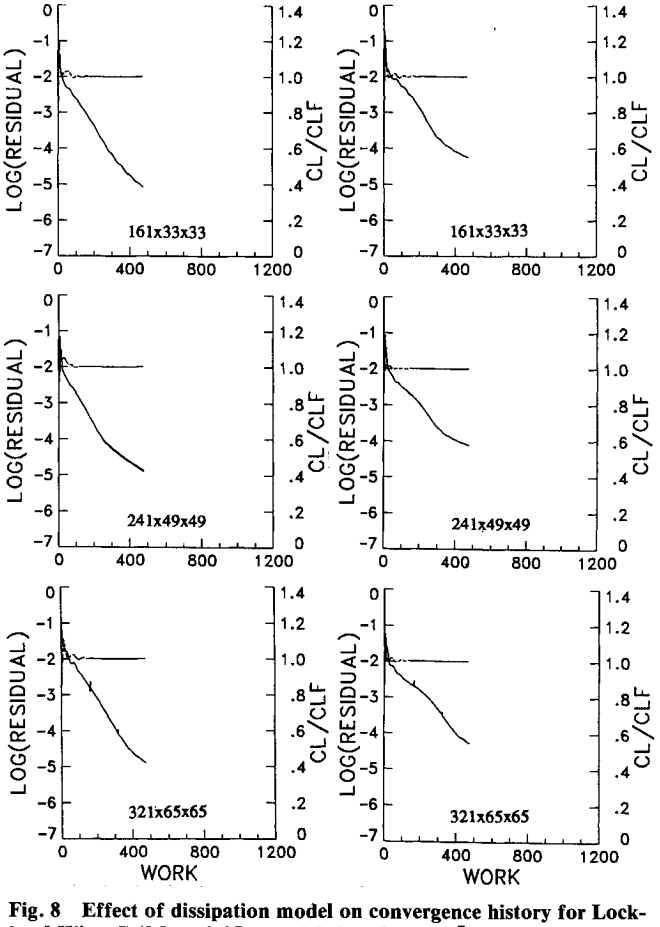

Fig. 8 Effect of dissipation model on convergence history for Lockheed Wing C ($M_\infty = 0.85$, $\alpha = 4.9$ deg, $Re_{\bar{c}} = 10^7$).

finest meshes exhibited inconsistent behavior with mesh refinement.

D. Convergence Properties

The preceding results clearly indicate that one can improve the accuracy of the numerical solutions by replacing the scalar dissipation model with a matrix dissipation model. However, there is a certain price to pay for achieving this improved accuracy in terms of computational costs, arising from the additional complexity of the dissipation model and a degradation of the temporal convergence to the steady state. An attempt is now made to quantify the additional computational cost involved in the use of the matrix-valued dissipation model.

A significant part of the additional operations associated with the matrix dissipation is due to the matrix multiplications required for obtaining the components of the dissipative terms, such as those given by Eq. (8). Turkel[7] had carefully examined the special form of the flux Jacobian matrices and the column vectors involved in these operations and derived a much simpler form for the products via regrouping of terms. This more efficient procedure, described in an earlier section of this paper, is employed in the computer code. The computational penalty associated with the matrix dissipation model for the cases presented here is found to be approximately a 20% increase in cpu time, per multigrid cycle.

In order to assess the additional cost due to differences in convergence rate, the variation of the lift coefficient normalized with its final converged value (CL/CLF) and the residual of the continuity equation are shown as a function of work units in Figs. 7 and 8, where one work unit represents the computational effort required for one fine mesh iteration. The convergence histories for the two test cases on the three different meshes used in this study are shown in these figures for both the scalar and matrix dissipation models. A small degradation in the convergence rate of the residuals is noted for the matrix dissipation model when compared to the scalar dissipation model. Although, within plotting accuracy, the lift convergence seems somewhat insensitive to the dissipation model, it also converges at a slower rate for the matrix dissipation model. Approximately 15–20% more work units are required for the matrix dissipation model to achieve the convergence level comparable to the scalar dissipation model, in addition to the 20% extra cpu time required per work unit. However, the matrix dissipation model produces a more cost-effective scheme, since the overall accuracy of the solutions with matrix dissipation is much better on a given mesh (Figs. 1–6), and one can employ coarser meshes to achieve a specified level of accuracy.

Concluding Remarks

The effect of replacing the scalar artificial dissipation model with a matrix-valued dissipation model on the accuracy of Navier-Stokes solutions for transonic flows has been investigated. In general, the numerical accuracy of the Navier-Stokes solutions is improved through the use of the matrix-valued dissipation model on a given size mesh. The additional cost that was incurred due to increased complexity and the degradation of the temporal convergence rate associated with the use of the matrix dissipation model is offset by the improved spatial accuracy. The resulting scheme is more cost-effective than the scalar dissipation-based scheme for achieving a specified level of accuracy for the two test cases considered here.

The central-difference scheme with the proposed matrix dissipation model is comparable in accuracy and arithmetic operations to a Roe type of upwind difference scheme and is simpler to implement in computer codes. In addition, the convergence rate for this scheme is quite good even on extremely fine meshes, which makes it very cost-effective.

Essentially grid-converged solutions have been obtained for both the pressure and surface skin-friction distributions for high Reynolds number, transonic flows over two different wing configurations. Whereas accurate pressure distributions

can be obtained on the finest meshes used in this study even with the scalar dissipation model, it is clear that a less dissipative scheme, such as the one designated here as the matrix-valued dissipation scheme, is required to obtain accurate and grid-converged solutions for the surface skin-friction distributions on mesh densities that are practical at this point in time. In addition, engineering accuracy can be obtained on relatively coarse meshes with the use of the matrix dissipation model.

References

[1]Vatsa, V. N., and Wedan, B. W., "Development of an Efficient Multigrid Code for 3-D Navier-Stokes Equations," AIAA Paper 89-1791, June 1989.

[2]Jameson, A., Schmidt, W., and Turkel, E., "Numerical Solutions of the Euler Equations by Finite Volume Methods Using Runge-Kutta Time-Stepping Schemes," AIAA Paper 81-1259, June 1981.

[3]Jameson, A., and Baker, T.J., "Solutions of the Euler Equations for Complex Configurations," AIAA Paper 83-1929, July 1983.

[4]Martinelli, L., "Calculation of Viscous Flows with Multigrid Methods," Ph.D. Dissertation, MAE Dept., Princeton Univ., Princeton, NJ, 1987.

[5]Swanson, R. C., and Turkel, E., "Artificial Dissipation and Central Difference Schemes for the Euler and Navier-Stokes Equations," AIAA Paper 87-1107, June 1987.

[6]Baldwin, B. S., and Lomax, H., "Thin Layer Approximation and Algebraic Model for Separated Turbulent Flows," AIAA Paper 78-257, Jan. 1978.

[7]Turkel, E., "Improving the Accuracy of Central Difference Schemes," *11th International Conference on Numerical Methods in Fluid Dynamics,* Lecture Notes in Physics, Vol. 323, Springer-Verlag, New York, 1988, pp. 586–591.

[8]van Leer, B., Thomas, J. L., Roe, P. L., and Newsome, R.W., "A Comparison of Numerical Flux Formulas for the Euler and Navier-Stokes Equations," AIAA Paper 87-1104, June 9–11, 1987.

[9]Vatsa, V. N., Thomas, J. L., and Wedan, B.W., "Navier-Stokes Computations of Prolate Spheroids at Angle of Attack," AIAA Paper 87-2627, Aug. 1987.

[10]Schimtt, V., and Charpin, F., "Pressure Distributions on the ONERA-M6 Wing at Transonic Mach Numbers," AGARD-AR- 138, May 1979, Ch. B-1.

[11]Hinson, B. L., and Burdges, K. P., "Acquisition and Application of Transonic Wing and Far-Field Test Data for Three-Dimensional Computational Method Evaluation," Lockheed Georgia Co., AFOSR-TR-80-0421, 1980.

[12]Garriz, J. A., Newman, P. A., Vatsa,V. N., Haigler, K. J., and Burdges, K. P., "Evaluation of Transonic Wall Interference Assessment and Corrections for Semi-Span Wing Data," AIAA Paper 90-1433, June 1990.

[13]Bonhaus, D., and Wornom, S. F., "Relative Efficiency and Accuracy of Two Navier-Stokes Codes for Simulating Attached Transonic Flow over Wings," AIAA Paper 90-3078, July 1990.

[14]Roe, P. L., "Approximate Riemann Solvers, Parameter Vectors and Difference Schemes," *Journal of Computational Ph*ysics, Vol. 43, No. 2, 1981, pp. 357–372.